Acta Oncologica, 2006; 45: 935–942

Taylor & Francis
Taylor & Francis Group

ORIGINAL ARTICLE

Comparison of respiratory surrogates for gated lung radiotherapy without internal fiducials

S. KORREMAN[1], H. MOSTAFAVI[2], Q-T LE[3] & A. BOYER[3]

[1]*Department of Radiation Oncology, Rigshospitalet, Copenhagen, Denmark,* [2]*Gintzon Technology Center, Varian Medical Systems, Mountain View, California, USA and* [3]*Department of Radiation Oncology, Stanford University School of Medicine, Stanford, California, USA*

Abstract
An investigation was carried out to compare the ability of two respiratory surrogates to mimic actual lung tumor motion during audio coaching. The investigation employed video clips acquired after patients had had fiducial markers implanted in lung tumors to be used for image-guided stereoscopic radiotherapy. The positions of the markers in the clips were measured within the video frames and used as the standard for tumor volume motion. An external marker was tracked optically during the fluoroscopic acquisitions. An image correlation technique was developed to compute a gating signal from the fluoroscopic images. The correlation gating trace was similar to the optical gating trace in the phase regions of the respiratory cycle used for gating. A cross correlation analysis and comparison of the external optical marker gating with internal fluoroscopic gating was performed. The fluoroscopic image correlation surrogate was found to be superior to the external optical surrogate in the AP-views in four out of six cases. In one of the remaining two cases, the two surrogates performed comparably, while in the last case, the external fiducial trace performed best. It was concluded that fluoroscopic gating based on correlation of native image features in the fluoroscopic images will be adequate for respiratory gating.

Non-small cell lung cancer (NSCLC) is a common neoplasm that, in general, is associated with poor long-term survival. Median survival of patients with unresectable tumors is approximately 6–8 months if untreated, and 11–13 months if aggressive chemotherapy and radiation are used [1]. These poor outcomes have led to the investigations of newer cytotoxic agents and more aggressive radiation therapy for the management of these tumors. Radiation is a widely accepted treatment for unresectable or inoperable NSCLC. Modern radiation therapy employs conformal fields and dose escalation to enhance tumor control, however further dose escalation with conventional radiation delivery techniques risks more injury to adjacent intrathoracic organs. The results of radiation dose escalation are discussed in several reviews, for instance [2,3]. Traditional efforts to increase radiation dose to thoracic tumors without risking normal tissue injury have generally required relatively invasive techniques such as interstitial brachytherapy or intraoperative radiotherapy (IORT). New techniques in external beam radiotherapy such as 3-D conformal and intensity-modulated radiotherapy provide a means to precisely shape the dose distributions to the shape of tumors. This results in redistributing the dose to surrounding normal tissues, reducing the normal tissue mean dose but increasing the normal tissue irradiated volume. This has been shown to improve radiation treatment outcomes in a number of cancer groups, such as head-and-neck cancers and prostate cancers [4,5]. High-precision radiation techniques are now widely applied to these cancer sites, as well as for other sites where respiratory motion is not an issue. Dosimetric studies of IMRT techniques for treating lung tumors have predicted reductions of the mean dose to the lung by 8% on average without consideration of respiration [6].

Stereotactic radiotherapy (STR) has been shown to be a highly effective treatment for brain metastases from NSCLC as well from other primary tumors. This suggests that selective small lung tumors, either primary or metastatic tumors, may be effectively controlled by similar focal high-dose STR. Wulf

Correspondence: S. Korreman, Department of Radiation Oncology, The Finsen Center 3994, Rigshospitalet, Blegdamsvej 9, DK-2100 Copenhagen Ø, Denmark. Tel: +45 35 45 39 06. Fax: +45 35 45 39 90. E-mail: stine.k@rh.dk

(Received 16 June 2006; accepted 11 July 2006)

ISSN 0284-186X print/ISSN 1651-226X online
DOI: 10.1080/02841860600917161

et al. used 3×10 Gy, 3×12–12.5 Gy or 1×26 Gy in a total of 61 patients with lung tumors and pulmonary metastases [7]. They reported a 12-month actuarial local control rate of 73% with 3×10 Gy, increasing to 97% with 3×12–12.5 Gy and 1×26 Gy. Uematsu et al. applied STR as either definitive treatment or as a boost in 50 patients with T1-2 NSCLC [8]. The doses used were 50–60 Gy given in 5–10 fractions delivered in 1–2 weeks. With a median follow-up of 36 months, the local control rate was 94% and the 3-year survival rate was 66%. No significant late toxicity was noted with STR except for six patients with temporary pleural pain and two with minor bone fracture.

However, for thoracic and abdominal cancers, the use of high-precision radiation is severely limited by breathing motion of both tumor and surrounding tissues. The respiratory trajectories taken by thoraco-abdominal anatomical structures may not move symmetrically between inhalation and exhalation and may lag in phase with respect to the contraction of the diaphragm. The relative amplitudes of the excursions of different structures may not be consistent day to day, depending on factors such as the patency of the lung parenchyma throughout a course of radiotherapy, hydration of the patient, and perhaps the contents of the stomach.

The integrated x-ray absorption through the thorax detected by a flat panel array produces image features that are directly related to the anatomy through which they pass. The motion of external markers may be less directly related to the internal organ motion.

Seppenwoolde [9] analyzed fluoroscopy clips of 20 lung cancer patients treated at the Department of Radiation Medicine, Hokkaido University School of Medicine, Sapporo, Japan. The system allows for 3-D tracking of high-density objects using four paired x-ray tubes and fluoroscopes mounted in the floor and ceiling around a linear accelerator. A 2 mm gold marker implanted in the tumor was tracked through the video clips with the aid of computer analysis of the frames comprising the video clips. The average amplitude of the tumor motion was greatest (12 ± 2 mm [SD]) in the cranial-caudal direction for tumors situated in the lower lobes of the lungs and not attached to rigid structures such as the chest wall or vertebrae. For the lateral and anterior-posterior directions, tumor motion was small both for upper- and lower-lobe tumors (2 ± 1 mm).

In order to ensure that the tumor is irradiated in all phases of the breathing cycle, a large margin has traditionally been added to radiation fields used to treat lung cancer. However, these large margins irradiate surrounding healthy tissues to high doses, thereby limiting the doses that one can deliver to tumors without an increased risk of radiation pneumonitis. A significant correlation has been demonstrated [10] between the mean dose to the lungs and the incidence of Grade 3 or higher pneumonitis. If breathing motion can be properly managed, high-precision radiotherapy with reduced field margins could improve clinical outcome for tumors in the thorax and abdomen. Respiratory motion of abdominal and thoracic cancers is therefore one of the largest impediments to optimizing radiotherapy for these cancers.

Previous studies of respiratory-correlated radiation treatment for breast cancers showed significant improvements with respect to sparing healthy lung and heart tissues from high dose irradiation [11,12]. The volume of the lung irradiated to more than 50% of the prescription dose can be reduced by approximately 25%, and irradiation of the heart can be almost entirely eliminated, while sufficient irradiation of the breast and regional lymph nodes is maintained. Yorke has calculated the dose distributions in lung using a relatively simple but conformal 6 MV treatment technique to compare deep inspiration breath holding with free-breathing using CT scans of five patients acquired under these two conditions [13]. She calculated that with the tumor volume stabilized by the deep inspiration breath holding, the dose to the tumor volume could be increased by 10% over the free-breathing condition for the same pulmonary and spinal toxicity. This result was obtained despite an extended penumbra due to increased electron transport in the low lung density created by the deep inspiration. A clinical study has demonstrated that by using deep inspiration breath holding it is feasible to escalate the prescribed dose to small lung tumors to 90 Gy using conventional fractionation without compromising the surrounding normal tissues [14,15].

However, these results are preliminary and the optimal approach for performing respiratory-correlated radiotherapy for tumors in the thorax or abdomen has not yet been well established. Means to manage respiratory motion include voluntary deep inspiration breath holding [14], forced breath holding [16], and gating [17]. Techniques for respiratory gating include the use of external markers, tracked by optical technology [17], radio-frequency passive coil excitation [18], and fluoroscopic tracking of internal markers (usually implanted radio-opaque fiducial "seeds") [19,20]. Radio-opaque markers implanted surgically under fluoroscopic or computerized tomography guidance provides a definitive means to locate the tumor target volume by using diagnostic quality x-rays. However, fiducial placement is not without risk,

especially in patients with poor lung function, and has been associated with hemoptysis and pneumothorax. In addition, fiducial-related hemorrhage can produce a radiographic blush around the tumor that can obfuscate the boundary of the clinical target volume. Implanted gold markers have also been observed to migrate from their original implant site [21]. Although a number of gating techniques employ external markers as surrogates for internal tumor motion, there is evidence that the tracking of external markers will not always follow the motion of internal tumors [22].

This study aims to investigate the correlation of two different surrogates – an external optical marker and native fluoroscopic image features – to tumor motion during coaching to improve breathing regularity.

Materials and methods

We conducted a feasibility study approved by the Stanford University Institutional Review Board to determine the maximal tolerated dose for single fraction STR in patients with lung tumors. Three to four radio-opaque fiducial markers were implanted in patients' lung tumors under CT guidance by an interventional radiologist. A subset of seven patients enrolled on these studies also consented to be imaged by fluoroscopy. Fluoroscopic image series, three consecutive movies in the anterior-posterior (AP) view followed by three consecutive movies in the medio-lateral (ML) view, of the respiratory motion of the markers within the tumors were acquired as video segments using a fluoroscope on radiotherapy simulators (Ximatron and Acuity, Varian Medical Systems, Palo Alto, CA). The images along with external marker motion measurements were acquired using the hardware and software tools provided in a real-time position management system (RPM™, Varian Medical Systems, Palo Alto, CA). An infrared tracker block was placed on the supine patients' xiphoid process during the acquisitions. The RPM™ system was set up to produce audio instructions to coach patients to attain a regular breathing pattern close to their natural cycle. Reflections of an infrared beam directed toward the reflector were captured by a video camera equipped with a narrow band-pass infrared filter. A tracking algorithm produced a quantitative measure of the anterior-posterior chest wall motion that was saved in a computer file to provide an indication of the amplitude and phase of respiration motion. At the same time a video clip was recorded consisting of digital images acquired from the simulators fluoroscopic system at a rate of 10 frames per second. The video frames were synchronized to the optical marker signal. The video clips were roughly 40 s long providing about 400 frames in which the motion of the radio-opaque markers could be observed over about six to ten respiratory cycles. Video clips were acquired from both the anterior/posterior and right/left lateral views for seven lung cancer patients. The video clips were processed using a template matching algorithm that tracked the pixel address of a selected marker over the $\sim$400 frames. The internal marker tracking algorithm was similar to the one described by Shirato et al. [20]. The pixel address of the marker in a given frame was converted to a measure of position in orthogonal coordinates (in units of centimeters) by calibration according to reticules in the fluoroscope images. The resulting respiratory traces were taken as the true tumor motion. In this study only the internal seed trace along the axis showing the largest respiratory motion (in most cases superior-inferior motion) was considered.

A surrogate respiratory trace based on native features in the fluoroscopic images was found as follows. A small region of interest (ROI) excluding the gold seeds but including an amount of tumor volume was defined manually in a selected frame in a clip. This ROI was used as a template for the image correlation algorithm. Thus the correlations depended entirely on native image features such as the tumor volume. In these cases, the slightly higher density of the lung tumors produced a feature that was visible against the lower density of the lung parynchma. The respiratory changes in this density within the ROI arising from tumor motion dominated the correlation traces. The algorithm correlated pixel values in the ROI template from the selected frame with the pixel values in ROIs of the same size and position in the rest of the frames in the clip. The frame selected for the reference ROI was at end expiration as determined by the internal seed displacement measure. The pixel indices in the video clip ranged from $I=1$ to $I=\mathrm{I}$ and from $j=1$ to $j=\mathrm{J}$ across the image in any frame of total size $\mathrm{I}\times\mathrm{J}$. Within a region of interest ($i,\ j\in ROI$) pixels indices ranged from $I=i_{min}$ to $I=i_{max}$ and from $j=j_{min}$ to $j=j_{max}$. The center of the ROI had pixel indices $i_0=(i_{max}-i_{min})/2$ and $j_0=(j_{max}-j_{min})/2$. Let the pixel values in the ROI in the reference frame be $R_{i,j,ref}$ at the pixel indices (i,j). Similarly, let $T_{i,j,k}$ be the pixel values at the pixel indices (i,j) for any frame number k in the video clip. Then the form of the correlation was

$$C_{i,j,k}=\frac{\sum_{i',j'\in ROI} R_{i',j',ref}\cdot T_{i-i',j-j',k}}{\sum_{i',j'\in ROI} R_{i',j',ref}\sum_{i',j'\in ROI} T_{i',j',k}}$$

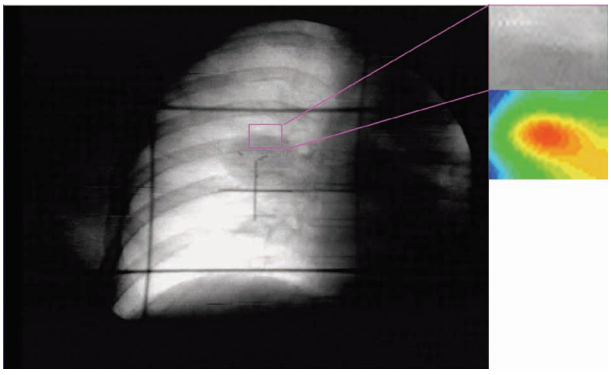

Figure 1. Correlation of the reference ROI with itself in the reference frame. A color map of correlation values (red indicating high correlation values) of the entire frame is shown on the right hand side. A correlation value of 1 is obtained at the center pixel of the ROI.

Since the correlation as computed here was normalized, the correlation of the reference ROI with itself must have a value of 1.00 at the center of the array at pixel values (i_0, j_0) as illustrated in Figure 1. Figure 1 contains the video fluoroscopic image over which the ROI has been overlaid as a rectangle. On the right hand side, the ROI and a color map of correlation values as defined above within the ROI is shown. The correlation value is 1.00 in the center of the ROI, and is shown in red in the color map.

In Figure 2, a test frame from the respiratory sequence is shown (the tumor image is lower than in Figure 1, corresponding to larger lung inflation). A correlation was computed in this frame within the same ROI bounds as in the reference frame. The correlation value was less than unity at the center of the test ROI because the correlation peak has moved off the center of the ROI in synchrony with the changes in the pixel values within the test ROI. The correlation value obtained in this manner is somewhat arbitrary. The pixels on which the correlation values are calculated are the accumulated projection

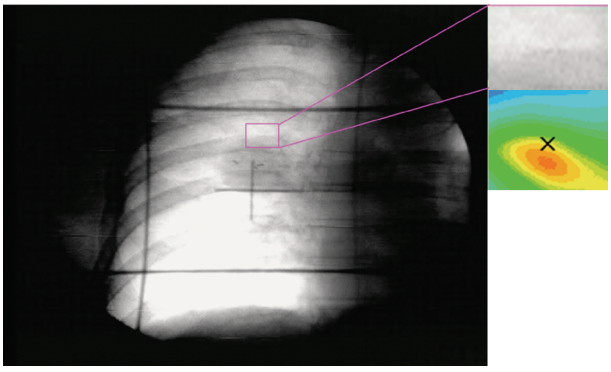

Figure 2. Correlation value $C_{i0,j0,k}$ of the $\mathrm{ROI}_{\mathrm{ref}}$ with the ROI in another frame, k, is taken at the center pixel of the array (at the x in the right hand side).

of x-rays passing through the patient. The motions of structures inside the pleural cavity and outside the pleural cavity both contribute to the detected pixel values. Changes in the pixel values from frame-to-frame are the result of the true tumor motion within the ROI as well as some distracting values resulting from motion of extrapleural structures. The correlation traces will probably never reach a value of 1 because from one respiration cycle to the next, the patient is never in exactly the same position and the noise in the system is never identical. Similarly, there is always some similarity between the ROI in a given frame and the ROI in the reference frame. Since most individuals tend to pause briefly in the end expiration phase, the correlation traces tend to have a slightly flattened top.

Calculation of this single value of the correlation array can be carried out quickly so that the algorithm is essentially real-time. If the frames are acquired at a rate of 10 frames per second, then each frame acquisition occurs within a 100 ms time window. Calculation of the single correlation value can be accomplished in a fraction of this time causing a minimal delay before acquisition of the next frame.

We sought a means to determine whether there is any significant difference between gating based on the RPM and the image correlation traces relative to the quantitative seed motion.

Cross correlation was performed between the gold seed traces and respectively the external fiducial traces and the image correlation traces with normalized correlation coefficients calculated as

$$R(d) = \frac{\sum_i [(x(i) - \mu_x)(y(i-d) - \mu_y)]}{\sqrt{\sum_i (x(i) - \mu_x)^2}\sqrt{\sum_i (y(i-d) - \mu_y)^2}},$$
$$\mu_x = \langle x(i) \rangle$$
$$\mu_y = \langle y(i) \rangle$$

The correlation coefficients are calculated for a series $d = \{-2.0, -1.9, \ldots, 0.0, 0.1, \ldots, 2.0\}$ seconds of delays. Maximum correlation coefficients are taken as a measure of the quality of the surrogates to mimic the actual tumor motion, and the delays of the maximum coefficients are reported. A delay time different from zero of the maximum correlation coefficient, is taken to indicate a phase lag between the surrogate respiratory trace and the actual tumor motion. A negative delay time corresponds to the surrogate signal lagging behind the internal seed trace.

Results

The image processing parts of the study, both with respect to the internal seed tracking and the image

correlation, were highly influenced by the image quality. In the AP fluoroscopic views, the image quality was good in all cases, however in one case the internal seeds had to be manually tracked due to overlay of the image reticules with the seed motion. In the ML fluoroscopic views, the seeds had to be entirely or partly manually tracked in several cases due to overlay of image reticules and/or poor image quality. The image correlation process was successful in six out of seven cases in the AP views. The lack of success in the one case was due to the location of the tumour in the periphery of the image, such that a suitable reference ROI for image correlation in the expiratory phase of breathing could not be identified. In the ML-views, the image correlation was successful in only three out of seven cases, again owing to poor image quality.

No image processing was performed prior to seed tracking or image correlation, so it is possible that a higher success rate could be attained, if more advanced image processing methods were used.

Plots of the external fiducial trace, the image correlation trace and the internal seed trace for two AP fluoroscopic video sequences for different patients are shown in Figure 3. The sequence depicted in Figure 3a is obtained from a patient with a very regular breathing pattern, whereas the one in Figure 3b is from a patient with an irregular breathing pattern. For the patient with a regular breathing pattern, the three traces are somewhat dissimilar in the end-inspiration and end-expiration plateaus. However they are nearly identical in the intervening phase regions in which gating thresholds are often applied. The image correlation trace is most similar to the gold seed trace in all phases by visual inspection, even in patients with irregular breathing pattern.

For the patient with irregular breathing in Figure 3, all three traces appear dissimilar in all points, but again the image correlation trace resembles the gold seed trace most. There is a phase lag between the external and the internal fiducial traces, and additionally there is not a clear relationship between the amplitudes of the two traces.

This general picture that the image correlation trace most resembles the internal fiducial trace, applies to all but one of the patients.

Tables I and II show the maximum cross correlation coefficients, $R(d)_{max}$, and corresponding delay times, d, for all patients and all movie clips, in respectively the AP and ML views, for both the external fiducial traces and the image correlation traces.

In the AP-views, for patients 1, 2, 3 and 5, the image correlation traces exhibit equal and higher correlation coefficients combined with the most stable delay times. For patient 6, the two traces perform comparably, while for patient 7, the external fiducial traces have the highest correlation values combined with stable delay times. For patient 4, the image correlation trace could not be processed, and the internal seeds were tracked manually.

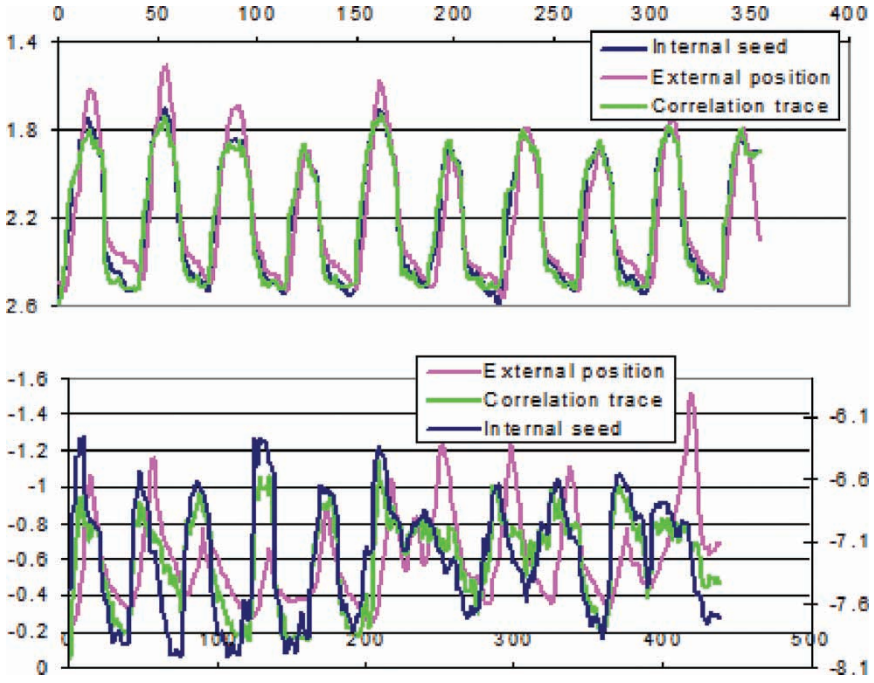

Figure 3. Examples of respiratory traces for two different patients; (a) a patient with a very regular breathing pattern, (b) a patient with an irregular breathing pattern. The gold seed and image correlation traces were obtained from AP fluoroscopic views. The vertical axes have arbitrary units, since the three traces are here scaled to have identical mean and standard deviations.

Table I. Maximum cross correlation coefficients and corresponding delay times for AP fluoroscopic views.

	External fiducial		Image correlation	
Patient/Movie	Corr. coeff.	Delay (s)	Corr. coeff.	Delay (s)
Patient 1				
1	0.94	0	0.96	0
2	0.96	−0.1	0.99	0
3	0.96	−0.1	0.94	0
Patient 2				
1	0.81	1.1	0.77	−0.1
2	0.49	1.4	0.9	0
3	0.68	1.9	0.6	−0.1
Patient 3				
1	0.67	1.3	0.72	1.2
Patient 4				
1	0.98	−0.1	–	–
2	0.9	−0.3	–	–
3	–	–	–	–
Patient 5				
1	0.9	0	0.87	0
2	0.83	−0.5	0.88	0.1
3	0.89	−0.6	0.89	0
Patient 6				
1	0.92	0	0.87	0.1
2	0.88	−0.1	0.77	0
3	0.78	−0.3	0.74	−0.2
Patient 7				
1	0.99	0	0.73	0.1
2	0.99	0	0.81	−0.1
3	0.98	0	0.86	0.1

A '–' indicates that correlation could not be performed, because of poor image processing. For patient 3 there was only one movie in the AP view.

Table II. Maximum cross correlation coefficients and corresponding delay times for ML fluoroscopic views.

	External fiducial		Image correlation	
Patient/Movie	Corr. coeff.	Delay (s)	Corr. coeff.	Delay (s)
Patient 1				
4	0.96	−0.1	0.97	0.1
5	0.98	−0.1	0.97	0
6	0.97	−0.1	0.98	0
Patient 3				
2	0.6	1.6	–	–
3	0.26	1.7	–	–
4	–	–	–	–
Patient 4				
4	0.83	−0.1	–	–
5	0.95	−0.1	–	–
6	–	–	–	–
Patient 5				
4	0.31	0.6	–	–
5	–	–	–	–
6	0.48	2	–	–
Patient 6				
4	0.94	−0.2	0.93	−0.1
5	0.92	−0.2	0.9	−0.1
6	0.86	−0.3	0.76	−0.2
Patient 7				
4	0.98	0	0.77	0.1
5	0.94	0	0.65	0.1
6	0.97	0	0.77	0.1

A '–' indicates that correlation could not be performed, because of poor image processing. The maximum axis of motion for patient 2 was mediolateral, which can not be seen in these views. Therefore no correlation values are indicated for this patient here.

In the ML-views, the image correlation traces and the external fiducial traces perform comparably for patients 1 and 6, while for patient 7, the external fiducial trace shows highest correlation coefficients combined with stable delay times.

It is noteworthy that the image correlation traces in general exhibit delay times closer to zero than the external fiducial traces. This is favorable for gating, because a non-zero phase lag between the motion surrogate and the actual tumor motion necessitates the use of phase gating for residual motion reduction. Phase gating again requires a phase prediction algorithm, which can only work well for patients with regular breathing patterns. Even in these cases such phase prediction algorithms will fail some of the time. It is also important to ensure that the phase lag is stable over time, so that an initial surrogate gating window can be trusted to produce a stable tumor position over an entire treatment fraction.

Discussion

The results given here indicate that image correlation on the fluoroscopic images can provide timing for gating that is adequate and in most cases equal or superior to that of an external marker. However, a good image quality is crucial for the success of this approach. On-line fluoroscopic imaging can be implemented using kilovoltage imaging integrated with the medical accelerator.

The application of kilovoltage imaging to the problems of patient positioning on medical linear accelerators has been investigated for several decades. The issue of configuration of the kilovoltage system with respect to the megavoltage treatment geometry has been investigated [23] and continues to be a matter of investigation. This investigation considered a single kilovoltage imaging system (a monoscopic system). The use of cone-beam CT may enable the accurate localization of lung tumors without using fiducial markers and may also enable the use of monoscopic respiratory gating.

The kilovoltage imaging systems employ a separate diagnostic energy x-ray generator and x-ray tube and an amorphous silicon flat panel digital x-ray image acquisition system. The imaging system can operate in a fluoroscopic mode in which images are acquired continuously at 30 frames per second and saved formatted as video clips. The flat panel array

receptor is sufficiently sensitive to form clear images at exposure rates of 20 nGy/s in the fluoroscopic mode. The gantry can rotate around isocenter in 60 s, acquiring 1800 frames or slower to acquire more frames. These frames can then be used as projections to reconstruct a cone-beam computerized tomography reconstruction.

The operation of the cone-beam CT system with respiratory gating would be as follows. The patient would be placed on the treatment table in an immobilization device and roughly aligned with laser side-lights. The operator would place the RPM external marker block on the patient's chest and the patient might wear video glasses to augment auditory coaching. The operator would select the CT option to move the x-ray tube and image receptor into the correct position for a half-fan cone-beam image acquisition. The RPM Gating system will be used to monitor the patient's breathing during the acquisition, and each projection will be given a label that reveals at which point in the cycle the projection was acquired. The projections will then be sorted into 6 to 8 bins across the respiratory cycle, and separate CT datasets will be reconstructed for each bin. The result will be a four-dimensional CT dataset consisting of 6 to 8 subsets, each at a different point in the breathing cycle. Data acquisition and reconstruction would take about 2–5 minutes. Patient positioning would be verified using a 3-D correlation between the reference data and the acquired data at a given phase of respiration. The dose and the acquisition time for a respiratory gated cone-beam CT will be greater than that for an ungated cone-beam acquisition by a factor of 6 to 8.

The process we envision developing can be described with the aid of Figure 4. A patient will have been positioned for treatment in the supine position in an immobilization device. The RPM system will be deployed with an external marker block placed on the patient's sternum. The RPM system will be initiated to begin audio coaching the patient to regularize his/her breathing. A gated cone-beam CT will then be acquired to verify the localization of the PTV. That having been done, the gantry and couch will be rotated to set up the first treatment beam. The RPM system will be initiated to begin audio coaching the patient to regularize their breathing. Referring to Figure 4, by frame 75, when a regular breathing pattern has been observed, the operator will energize the kilovoltage x-ray system just after frame 100 and the algorithm will pick up a reference ROI in the expiration phase at about frame 120. The correlation value will then be computed for subsequent frames, giving the correlation curve depicted in the top of Figure 4. At frame 180 the operator can see that a regular correlation curve is being generated and initiates the treatment beam. When the correlation value rises above the trigger level (depicted as a dashed line in Figure 4), the beam is turned on (depicted as the blocks in Figure 4). For the purpose of illustration, assume the following optimistic scenario: 10 treatment beams are used to deliver a total prescribed dose of 25 Gy, by delivering about 2.5 Gy each (requiring about 333 MU). For a dose rate of 1 000 MU/min, the total beam time for one field would be 20 s. In the example in Figure 4, the respiratory cycle has a period of about 6 s. Assuming the beam is gated on an average of 4 s during each respiratory cycle, a single beam direction would be gated on five times as depicted in Figure 4. The total time required to establish the gating pattern and treat at this gantry angle would have been less than 1 min. Once the required number of MU have been delivered under fluoroscopic respiratory gating, the gantry angle and couch angle for the next beam will be set automatically and the sequence will be repeated for the next beam. Each beam of the 10 beams will require

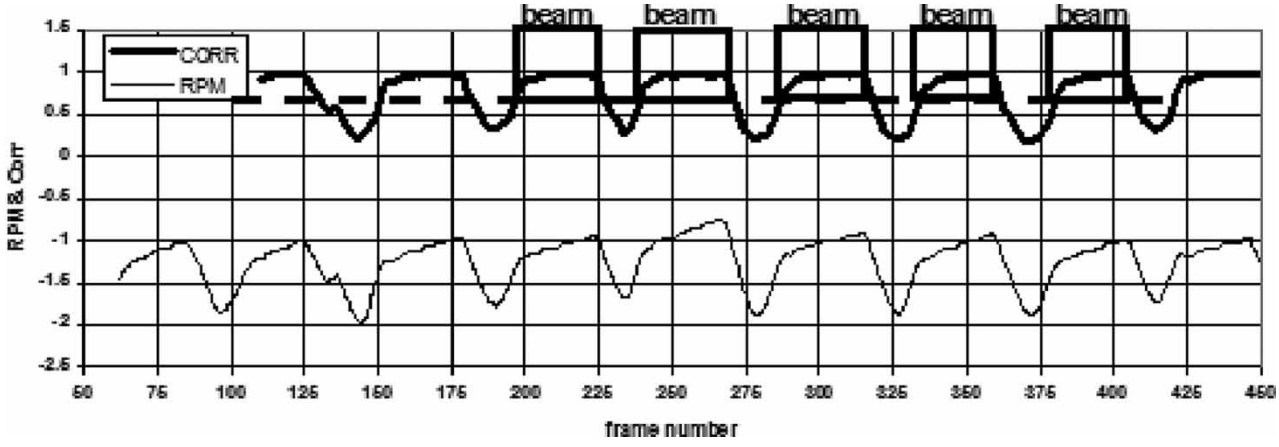

Figure 4. A schematic of the fluoroscopic gating process. The lower curve is the RPM signal derived from the external marker. The upper curve is the fluoroscopic gating signal derived from correlation of a ROI in the fluoroscopic image.

about 1 min to deliver, so the total treatment would be delivered in about 10 min.

For fractionated treatment, the entire imaging procedure would have to be repeated on each treatment day, and the total dose to the patient from imaging procedures would have to be considered and minimized.

Conclusion

We have found that native fluoroscopic image features can provide a surrogate for respiratory tumor motion adequate for gating purposes. In terms of cross correlation coefficients combined with delay times, the image correlation method performed superior to an external marker in four out of six cases. Furthermore, we have sketched a practical approach to an image-based respiratory gating system utilizing on-line respiratory correlated cone-beam CT imaging.

Acknowledgements

The authors would like to thank Bill Loo, Gary Luxton, Todd Pawlicki and Edward Graves at Stanford University School of Medicine, CA, for fruitful collaboration.

This study was partially funded by a research grant from Varian Medical Systems, Inc.

References

[1] John MJ. Radiotherapy and chemotherapy. Textbook of Radiation Oncology. Leibel SA, Phillips TL. Philadelphia: W.B. Saunders Co; 1998. p 69–89.

[2] Donat V, Zurlo A, Bonfili P, et al. Hypofractionated radiation therapy for inoperable advanced Stage I Non-Small Cell Lung Cancer. Tumori 1999;85:174–6.

[3] Sause W, Scott CH, Taylor S IV. Radiation Therapy Oncology Group (RTOG) 88-08 and Eastern Cooperative Oncology Group (ECOG) 4588: Preliminary results of a phase III trial in regionally advanced, unresectable non-small-cell lung carcinoma. J Natl Cancer Inst 1995;87:198–205.

[4] Lee N, Xia P, Fischbein J, et al. Intensity-modulated radiation therapy for head-and-neck cancer: The UCSF experience focusing on target volume delineation. Int J Radiat Oncol Biol Phys 2003;57:49–60.

[5] Zelefsky MJ, Fuks Z, Hunt M, et al. High-dose intensity-modulated radiation therapy for prostate cancer: Early toxicity and biochemical outcome in 772 patients. Int J Radiat Oncol Biol Phys 2002;53:1111–6.

[6] Liu H, Wang X, Dong L, et al. Feasibility of sparing lung and other thoracic structures with intensity-modulated radiotherapy for non-small-cell lung cancer. Int J Radiat Oncol Biol Phys 2004;58:1268–79.

[7] Wulf J, Haedinger U, Oppitz U, et al. Stereotactic radiotherapy for primary lung cancer and pulmonary metastases: A non-invasive treatment approach in medically inoperable patients. Int J Radiat Oncol Biol Phys 2004;60:186–96.

[8] Uematsu M, Shioda A, Suda A, et al. Computed tomography-guided frameless stereotactic radiotherapy for stage I non-small-cell lung cancer: A 5-year experience. Int J Radiat Oncol Biol Phys 2001;51:666–70.

[9] Seppenwoolde Y, Shirato H, Kitamura K, et al. Precise and real-time measurement of 3D tumor motion in lung due to breathing and heartbeat, measured during radiotherapy. Int J Radiat Oncol Biol Phys 2002;53:822–34.

[10] Yorke ED, Wang L, Rosenzweig KE, et al. Evaluation of deep inspiration breath-hold lung treatment plans with Monte Carlo dose calculation. Int J Radiat Oncol Biol Phys 2002;53:1058–70.

[11] Pedersen AN, Korreman S, Nystrom H, et al. Breathing adapted radiotherapy of breast cancer: Reduction of cardiac and pulmonary doses using voluntary inspiration breath-hold. Radiother Oncol 2004;72:53–60.

[12] Korreman SS, Pedersen AN, Nottrup TJ, et al. Breathing adapted radiotherapy for breast cancer: Comparison of free breathing gating with the breath-hold technique. Radiother Oncol 2005;76:311–8.

[13] Yorke ED, Jackson A, Rosenzweig KE, et al. Dose-volume factors contributing to the incidence of radiation pneumonitis in non-small-cell lung cancer patients treated with three-dimensional conformal radiation therapy. Int J Radiat Oncol Biol Phys 2002;54:329–39.

[14] Rosenzweig KE, Hanley J, Mah D, et al. The deep inspiration breath-hold technique in the treatment of inoperable non-small-cell lung cancer. Int J Radiat Oncol Biol Phys 2000;48:81–7.

[15] Chapman JD, Bradley JD, Eary JF, et al. Molecular (functional) imaging for radiotherapy applications: An RTOG symposium. Int J Radiat Oncol Biol Phys 2003;55:294–301.

[16] Wong JW, Sharpe MB, Jaffray DA, et al. The use of active breathing control (ABC) to reduce margin for breathing motion. Int J Radiat Oncol Biol Phys 1999;44:911–9.

[17] Minohara S, Kanai T, Endo M, et al. Respiratory gated irradiation system for heavy-ion radiotherapy. Int J Radiat Oncol Biol Phys 2000;47:1097–103.

[18] Seiler PG, Blattmann H, Kirsch S, et al. A novel tracking technique for the continuous precise measurement of tumour positions in conformal radiotherapy. Phys Med Biol 2000;45:N103–10.

[19] Shirato H, Shimizu S, Kunieda T, et al. Physical aspects of a real-time tumor-tracking system for gated radiotherapy. Int J Radiat Oncol Biol Phys 2000;48:1187–95.

[20] Shirato H, Shimizu S, Kitamura K, et al. Four-dimensional treatment planning and fluoroscopic real-time tumor tracking radiotherapy for moving tumor. Int J Radiat Oncol Biol Phys 2000;48:435–42.

[21] Kitamura K, Shirato H, Shimizu S. Migration of the internal fiducial gold marker implanted into prostate and liver treated with real-time tumour tracking radiation treatment (RTRT). Int J Radiat Oncol Biol Phys 2000;48:343–4.

[22] Ozhasoglu C, Murphy MJ. Issues in respiratory motion compensation during external-beam radiotherapy. Int J Radiat Oncol Biol Phys 2002;52:1389–99.

[23] Berbeco R, Jiang S, Sharpa GC, et al. Integrated Radiotherapy Treatment Planning System (IRIS): Design considerations of tumour tracking with linac gantry-mounted diagnostic x-ray systems with flat-panel detectors. Phys Med Biol 2004;49:243–55.